First light and reionization epoch simulations (FLARES) V : the redshift frontier

Wilkins, Stephen M.

2023-02

Wilkins , S M , Vijayan , A P , Lovell , C C , Roper , W J , Irodotou , D , Caruana , J , Seeyave , L T C , Kuusisto , J K , Thomas , P A & Parris , S A K 2023 , ' First light and reionization epoch simulations (FLARES) V : the redshift frontier ' , Monthly Notices of the Royal Astronomical Society , vol. 519 , no. 2 , pp. 3118-3128 . https://doi.org/10.1093/mnras/stac3280

http://hdl.handle.net/10138/356937
https://doi.org/10.1093/mnras/stac3280

Monthly Notices of the ROYAL ASTRONOMICAL SOCIETY

MNRAS **519,** 3118–3128 (2023) https://doi.org/10.1093/mnras/stac3280
Advance Access publication 2022 November 17

First light and reionization epoch simulations (FLARES) V: the redshift frontier

Stephen M. Wilkins [1,2★] Aswin P. Vijayan [1,3,4] Christopher C. Lovell [1,5] William J. Roper [1] Dimitrios Irodotou [1,6] Joseph Caruana,[2,7] Louise T. C. Seeyave,[1] Jussi K. Kuusisto,[1] Peter A. Thomas [1] and Shedeur A. K. Parris[1]

[1]*Astronomy Centre, University of Sussex, Falmer, Brighton BN1 9QH, UK*
[2]*Institute of Space Sciences and Astronomy, University of Malta, Msida MSD 2080, Malta*
[3]*Cosmic Dawn Center (DAWN)*
[4]*DTU-Space, Technical University of Denmark, Elektrovej 327, DK-2800 Kgs. Lyngby, Denmark*
[5]*Centre for Astrophysics Research, School of Physics, Astronomy & Mathematics, University of Hertfordshire, Hatfield AL10 9AB, UK*
[6]*Department of Physics, University of Helsinki, Gustaf Hällströmin katu 2, FI-00014, Helsinki, Finland*
[7]*Department of Physics, University of Malta, Msida MSD 2080, Malta*

Accepted 2022 October 26. Received 2022 October 24; in original form 2022 April 20

ABSTRACT

JWST is set to transform many areas of astronomy, one of the most exciting is the expansion of the redshift frontier to $z > 10$. In its first year, alone *JWST* should discover hundreds of galaxies, dwarfing the handful currently known. To prepare for these powerful observational constraints, we use the First Light And Reionization Epoch simulations (FLARES) to predict the physical and observational properties of the $z > 10$ population of galaxies accessible to *JWST*. This is the first time such predictions have been made using a hydrodynamical model validated at low redshift. Our predictions at $z = 10$ are broadly in agreement with current observational constraints on the far-UV luminosity function and UV continuum slope β, though the observational uncertainties are large. We note tension with recent constraints $z \sim 13$ from Harikane et al. (2021) – compared to these constraints, FLARES predicts objects with the same space density should have an order-of-magnitude lower luminosity, though this is mitigated slightly if dust attenuation is negligible in these systems. Our predictions suggest that in *JWST*'s first cycle alone, around 600 galaxies should be identified at $z > 10$, with the first small samples available at $z > 13$.

Key words: galaxies: evolution – galaxies: formation – galaxies: general – galaxies: high-redshift – galaxies: photometry.

1 INTRODUCTION

Identifying and characterizing the first generation of galaxies is one of the core aims of modern extragalactic astronomy. Doing so will provide the essential constraints to galaxy formation models, helping us elucidate the key physics of early galaxy formation and evolution (Dayal & Ferrara 2018; Robertson 2021).

Over the last 15 yr, remarkable progress has been made in studying the distant Universe, with >1000 candidate galaxies now identified at $z = 6$–10 (e.g. Bouwens et al. 2021). These have come pre-dominantly from the analysis of deep near-infrared (near-IR) observations from Wide Field Camera 3 (WFC3) on the *Hubble Space Telescope* (e.g. Bouwens et al. 2010; Bunker et al. 2010; McLure et al. 2010; Wilkins et al. 2011; Finkelstein et al. 2015; Bouwens et al. 2021), with a small but growing sample of bright sources, more amenable to multiwavelength follow-up, identified from ground-based imaging (e.g. Bowler et al. 2015). A number of these candidates have now been confirmed by spectroscopy, targeting Ly α (e.g Stark et al. 2010; Curtis-Lake et al. 2012; Caruana et al. 2014; Pentericci et al. 2014; Schenker et al. 2014; Stark et al. 2017; Mason et al. 2019) or far-IR lines (e.g Knudsen et al. 2016; Pentericci et al. 2016; Hashimoto et al. 2019).

While the vast majority of sources are at lower-redshift, a handful of objects have now been detected at $z > 10$, often combining *Hubble* and *Spitzer* observations. These include the surprisingly bright galaxy GN-z11 (Oesch et al. 2016) and more recently a pair of candidates at $z \sim 13$ (Harikane et al. 2021). With the successful launch of *JWST*, these sources look set to be only the first of many identified at $z > 10$ (Robertson 2021). *JWST* offers the sensitivity, survey efficiency, and wavelength coverage to push well beyond the current redshift frontier. In addition, *JWST* will provide rest-frame ultraviolet (UV) spectroscopy, allowing the confirmation of sources and the accurate measurement of many key physical properties. With the first results from *JWST* imminent, it is essential that we have theoretical predictions in place to allow us to interpret these revolutionary observations.

Theoretical predictions for the high-redshift Universe are available from a variety of modelling approaches. These include semi-empirical methods (e.g. Mason, Trenti & Treu 2015; Behroozi et al. 2020) and semi-analytical models (e.g. Clay et al. 2015; Poole et al.

★ E-mail: S.Wilkins@sussex.ac.uk

2016; Yung et al. 2019; Hutter et al. 2021). However, our most complete understanding comes from hydrodynamical simulations (e.g Khandai et al. 2012; Feng et al. 2016; Vogelsberger et al. 2020; Ni et al. 2022), particularly those incorporating full radiative transfer (RT; e.g. O'Shea et al. 2015; Ocvirk et al. 2016, 2020; Rosdahl et al. 2018; Kannan et al. 2022).

The main drawback of hydrodynamical simulations – especially those including RT – is that they are computationally expensive, limiting their volume, resolution, and/or redshift end point. This is a particular problem at very high redshift, where the source density is so low that simulations comparable to, and ideally much larger, observational surveys are essential to yield useful statistical predictions. Indeed, flagship cosmological simulations that have been validated at low-redshift, like EAGLE (Crain et al. 2015; Schaye et al. 2015), SIMBA (Davé et al. 2019), ILLUSTRIS (Genel et al. 2014; Vogelsberger et al. 2014a, b; Sijacki et al. 2015), and ILLUSTRIS-TNG (Naima(Marinacci et al. 2018; Naiman et al. 2018; Nelson et al. 2018; Pillepich et al. 2018; Springel et al. 2018) fail to pass this threshold, with only a small number of observationally accessible sources at $z > 10$.

One solution is to carry out much larger simulations, but limited to high-redshift. This is a strategy implemented by, e.g. MASSIVEBLACK (Khandai et al. 2012), BLUETIDES (Feng et al. 2016; Wilkins et al. 2017), and ASTRID (Ni et al. 2022). An alternative strategy is to *re-simulate* a range of environments drawn from a very large low-resolution parent simulation (e.g. Crain et al. 2009). This has the advantage of more efficiently allowing us to extend the dynamic range (see discussion in Lovell et al. 2021). These individual re-simulations are also much smaller than single large boxes, allowing wider and more efficient use of HPC systems. The chief disadvantages are the loss of most clustering information and the requirement to carefully understand the weightings of the individual simulations to obtain the correct statistical properties of the galaxy population. Machine learning approaches may allow us to overcome some of these limitations (e.g. Bernardini et al. 2022; Lovell et al. 2022)

Re-simulations of multiple regions is utilized in the First Light And Reionization Epoch simulations (FLARES) project. FLARES combines the validated at $z = 0$ EAGLE physics model with a re-simulation strategy yielding a much larger effective volume and dynamic range. Compared to the $(100\,\mathrm{Mpc})^3$ EAGLE reference simulation, FLARES contains 10–100$\times$ as many high-redshift galaxies. In this article, we use FLARES to make predictions for the galaxy population at $z > 10$, building on earlier work focused at $z = 5$–10 (Lovell et al. 2021; Vijayan et al. 2021, 2022; Roper et al. 2022).

This article is organized as follows: in Section 2, we briefly describe the FLARES project. In Section 3, we explore the physical properties of galaxies at $z > 10$, and in Section 4, explore their observational properties, including the UV luminosity function (LF) and forecasts for upcoming surveys (Section 4.1), the UV continuum slope β (Section 4.3), UV emission lines (Section 4.4), and the UV – optical colours (Section 4.5). Finally, in Section 5, we present our conclusions.

2 THE FIRST LIGHT AND REIONIZATION EPOCH SIMULATIONS

In this study, we make use of the FLARES (Lovell et al. 2021; Vijayan et al. 2021). FLARES is a suite of 40 spherical re-simulations, 14 h^{-1} Mpc in radius, of regions selected from a large $(3.2\,\mathrm{Gpc})^3$ dark matter-only simulation. The regions selected to re-simulate span a range of environments: (at $z \approx 4.7$) $\log_{10}(1 + \delta_{14}) = [-0.3, 0.3]$[1] with over-representation of the extremes of the density contrast distribution.

FLARES adopts the AGNdT9 variant of the EAGLE simulation project (Crain et al. 2015; Schaye et al. 2015). The AGNdT9 variant implements a higher heating temperature from active galactic nuclei compared to the reference EAGLE run, thus producing more energetic, less frequent feedback events. The AGNdT9 variant was chosen to align FLARES with the Cluster-EAGLE project (Barnes et al. 2017). However, this produces negligible changes relative to the standard *reference* variant in the relatively low halo-mass regime probed by FLARES. This, and other more extreme, changes to the model are explored in a work in preparation. We adopt identical resolution to the fiducial EAGLE simulation, i.e. dark matter and initial gas particle masses of $\mathrm{m_{dm}} = 9.7 \times 10^6 \mathrm{M_\odot}$ and $\mathrm{m_g} = 1.8 \times 10^6\ \mathrm{M_\odot}$, respectively, and a softening length of 2.66 ckpc. As with the original EAGLE simulations, we assume $\Omega_m = 0.307$, $\Omega_\Lambda = 0.693$, and $h = 0.6777$ based on results from Planck Collaboration (2014).

Galaxies in FLARES are first identified as groups via the Friends-Of-Friends (Davis et al. 1985) algorithm, and subsequently subdivided into bound groups with the SUBFIND (Springel et al. 2001; Dolag et al. 2009) algorithm. When measuring properties, we use 30 kpc radius apertures, centred on the most bound particle of each subgroup.

2.1 Spectral energy distribution modelling

Key to making observational predictions is the spectral energy distribution (SED) modelling applied to the simulation outputs. The SED modelling approach is presented in Vijayan et al. (2021), broadly following the approach developed by Wilkins et al. (2013b, 2016c, 2018, 2020), with modifications to the dust treatment. In short, we begin by associating each star particle with *pure stellar* SED using v2.2.1 of the Binary Population and Spectral Synthesis (Stanway & Eldridge 2018) stellar population-synthesis model assuming a Chabrier (2003) initial mass function (IMF). We then associate each star particle with H II region giving rise to nebular continuum and line emission. Specifically, we follow the approach detailed in Wilkins et al. (2020), in which the pure stellar spectrum is processed with the `cloudy` photo-ionization code (Ferland et al. 2017).

We account for the effects of dust attenuation in both the birth clouds of young stellar populations and the interstellar medium (ISM). The latter is accounted for using a line-of-sight (LOS) model similar to that described in Wilkins et al. (2018). In this model, we treat stellar particles as emitters along a LOS and account for the attenuation due to gas particles that intersect this LOS. To do this, we determine the metal column density and convert this to a dust optical depth using the fitting function for the dust-to-metal ratio presented in Vijayan et al. (2019), implemented as follows:

$$\tau_{\mathrm{ISM,V}}(x, y) = \mathrm{DTM}\,\kappa_{\mathrm{ISM}}\,\Sigma\,(x, y), \quad (1)$$

where $\tau_{\mathrm{ISM,\,V}}(x, y)$ and $\Sigma\,(x,\ y)$ are the V-band (550nm) optical-depth and integrated metal column density, respectively, of the intervening diffuse ISM, along the LOS at position (x,y) of the star particle. $\kappa_{\mathrm{ISM}} = 0.0795$ is a proportionality constant, chosen to match the rest-frame far-UV (1500Å) LF to the observed UV LF from Bouwens et al. (2015) at $z = 5$.

[1] Where δ_{14} is the density contrast measured within the resimulation volume size.

For the attenuation due to the birth cloud component, we scale it with the star particle metallicity, described as follows:

$$\tau_{\rm BC,V}(x,\,y) = \begin{cases} \kappa_{\rm BC}({\rm Z}_\star/0.01) & {\rm t} \leq 10^7{\rm yr} \\ 0 & {\rm t} > 10^7{\rm yr}\,, \end{cases} \quad (2)$$

where $\tau_{\rm BC,\,V}(x, y)$ is the V-band optical-depth due to the stellar birth-cloud and $\rm Z_\star$ is the smoothed metallicity of the young stellar particle. $\kappa_{\rm BC} = 1.0$, similar to $\kappa_{\rm ISM}$, is a normalization factor, chosen to match the UV-continuum slope observations from Bouwens et al. (2012, 2014) at $z = 5$ and the [O III]λ4959, 5007 + Hβ equivalent width distribution at $z = 8$ from De Barros et al. (2019a). In fixing the values of $\kappa_{\rm ISM}$ and $\kappa_{\rm BC}$ for all redshifts, there is an implicit assumption of no evolution in the general properties of the dust grains in galaxies, such as the average grain size, shape, and composition. We link the optical-depth in the V-band to other wavelengths using a simple power-law relation:

$$\tau_\lambda = (\tau_{\rm ISM} + \tau_{\rm BC}) \times (\lambda/550{\rm nm})^{-1}\,, \quad (3)$$

whose form generates an attenuation curve for a stellar particle flatter in the UV than the Small Magellanic Cloud curve (Pei 1992), but not as flat as the Calzetti et al. (2000) curve. It should be noted that the resultant attenuation curve can acquire different forms based on the star-dust geometry within a galaxy. This will be explored in a future work. This LOS model differs from using a uniform screen of dust across a galaxy (usually assumed in SED fitting of observed galaxies). We refer the interested readers to sections 2.3 and 2.4 and appendix A of Vijayan et al. (2021) for an in-depth discussion of the photometry generation in FLARES.

Since this model is based on extrapolation from lower-redshift, its applicability to $z > 10$ is highly uncertain and it is possible this model overestimates the amount of dust attenuation at these redshifts. For this reason, we also present intrinsic quantities throughout this work and are confident that these and our dust-attenuated quantities should bracket the dust modelling uncertainty.

2.2 Comparison to EAGLE

The core objective of FLARES is to expand both number and dynamic range of simulated galaxies at $z > 5$ compared to the EAGLE reference simulation. The number of galaxies in both FLARES and EAGLE with stellar mass greater than $\in \{10^8, 10^9, 10^{10}, \text{and } 10^{11}\}$ $\rm M_\odot$ at $z > 5$ are shown in Fig. 1. At $z = 10$, FLARES contains 100× (10×) as many galaxies as EAGLE with $M_\star > 10^9\,\rm M_\odot$ ($M_\star > 10^8\,\rm M_\odot$). At $z = 10$, FLARES contains ∼1000 galaxies at $M_\star > 10^8\,\rm M_\odot$, dropping to 10 by $z = 15$.

2.3 Environmental dependence

A key feature of FLARES is the explicit simulation of a wide range of environments with $\log_{10}[1 + \delta_{14}(z = 4.7)] \approx [-0.3, 0.3]$. In Lovell et al. (2021), we showed that the galaxy stellar mass function, and thus the total number of galaxies above a mass threshold, was extremely sensitive to the environment. A consequence of this, and the low number density of galaxies at $z > 10$, is that the vast majority of our simulated galaxies are in overdense regions, as shown in Fig. 2. At $z = 15$, only one simulation with $\delta < 0.5$ contains any galaxies. Since each simulation is appropriately weighted (see Lovell et al. 2021), the lack of any galaxies in many density contrast bins should not affect distribution functions like the galaxy stellar mass function or UV LF. However, if galaxy scaling relationships are sensitive to the environment, even the appropriately weighted relations could be

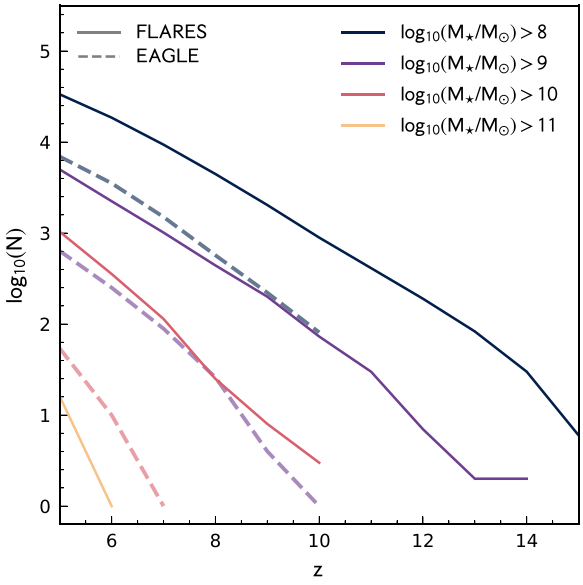

Figure 1. The number of galaxies in EAGLE (dashed line) and FLARES (solid line) at $z > 5$ above various stellar mass limits.

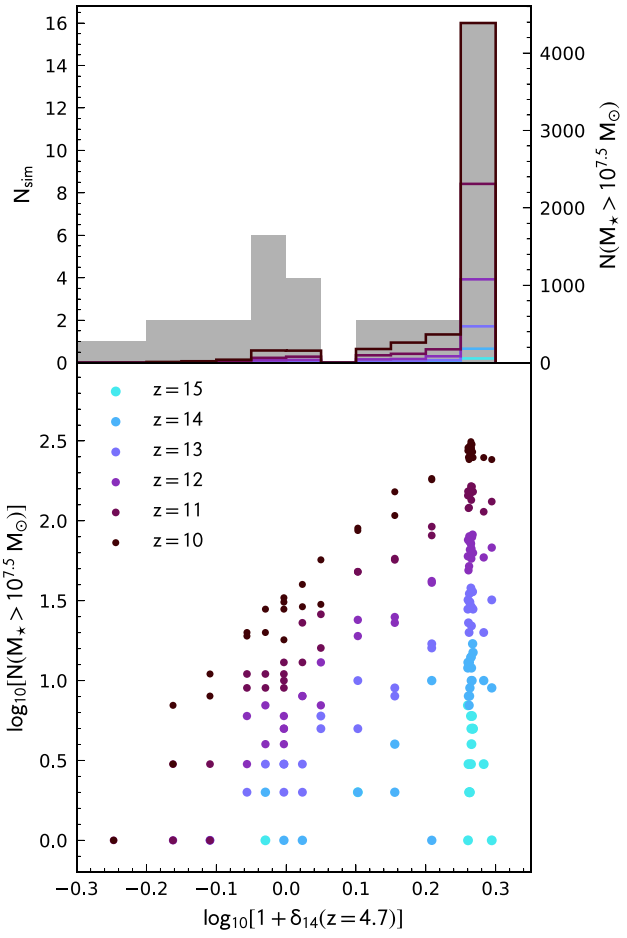

Figure 2. Bottom panel: The number of $M_\star > 10^{7.5}\,\rm M_\odot$ galaxies in each individual simulation as a function of density contrast. Top panel: The number of individual simulations (grey filled histogram) and $M_\star > 10^{7.5}\,\rm M_\odot$ galaxies in density contrast bins.

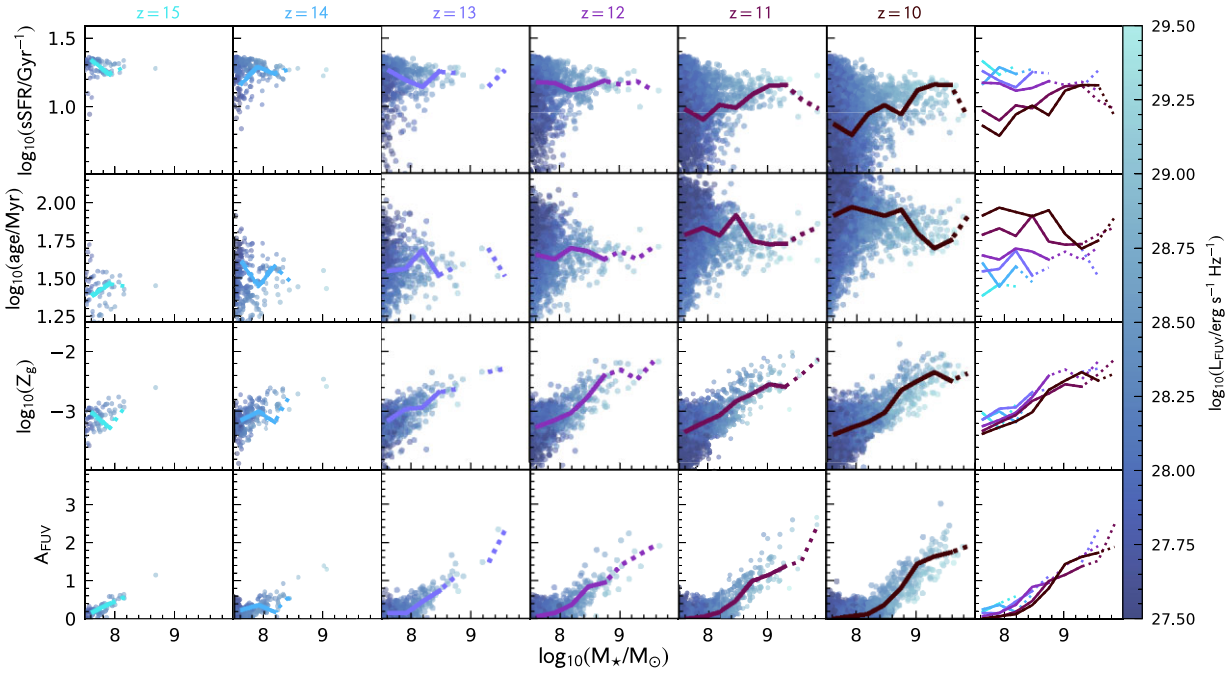

Figure 3. The predicted physical properties as a function of stellar mass at $z = 15 \rightarrow 10$. The line on each panel shows the weighted median, i.e. accounting for the statistical weights of each re-simulation. When the number of galaxies in each bin falls below 10, the median is denoted by a dotted line. The final panel summarizes the redshift evolution of the median. Individual galaxies are coloured by their far-UV luminosity.

biased. Fortunately, Lovell et al. (2021) found no significant evidence of environmental dependence in the key scaling relations.

3 PHYSICAL PROPERTIES

We begin by exploring a selection of key physical properties of galaxies at $z > 10$. In Fig. 3, we show the relationship between stellar mass and the specific star formation rate, age, gas-phase metallicity, and far-UV dust attenuation. At present, there are no observational constraints for these properties but this should soon change.

The relationship between stellar mass and specific star formation rate is predicted to be fairly flat, though with significant redshift evolution of the normalization. Similarly, the average age – defined here as the time since its stellar mass was half its current value – is flat with stellar mass but evolves strongly with redshift. At $z = 10$, the average age is predicted to be ≈20 Myr rising to almost ≈100 Myr at $z = 10$.

On the other hand, the gas-phase metallicity Z_g shows a significant trend with stellar mass but little redshift evolution. Similarly, we see a strong trend between the far-UV attenuation and stellar mass but little redshift evolution. Given the gas-phase metallicity trends, this is unsurprising since the attenuation in FLARES is related to surface density of metals.

3.1 Mass-to-light ratio

One of the most fundamental properties is the mapping between stellar mass and the (dust-attenuated) far-UV luminosity. This encodes the star formation and metal enrichment history of each galaxy in addition to reprocessing by dust and gas. This relationship is shown in Fig. 4. At $M_\star < 10^{8.5}\,\mathrm{M}_\odot$, this relationship is close to linear; at high-masses, however, the luminosity falls below the linear expectation. This is pre-dominantly due to the effects of dust, but is also affected by the higher stellar metallicities in the most massive galaxies. The scatter in this relationship is ≈0.2 dex independent of redshift and stellar mass.

4 OBSERVATIONAL PROPERTIES

We now turn our attention to some of the properties of galaxies that can be observed at $z > 10$. *JWST* will, for the first time, provide deep >2 μm imaging and spectroscopy, allowing us to measure several properties, including the rest-frame UV luminosity (and thus LF), the UV continuum slope, UV emission lines, and potentially even UV – optical colours via MIRI imaging. Model SEDs of star-forming galaxies at $z = 10$ and $z = 15$ are shown, alongside the *JWST* filter transmission functions in Fig. 5.

4.1 Far-UV luminosity function

The rest-frame far-UV LF is one of the key statistical descriptions of the galaxy population at high-redshift. This is pre-dominantly due to its accessibility but also the fact that the observed UV light traces both unobscured star formation (Kennicutt & Evans 2012; Wilkins, Lovell & Stanway 2019) and the production of ionising photons (Wilkins et al. 2016b). The far-UV LF has now been measured extensively to $z \sim 8$ with tentative constraints at ∼10 (e.g McLeod, McLure & Dunlop 2016; Oesch et al. 2018; Finkelstein et al. 2021) and more recently at $z \sim 13$ (Harikane et al. 2021).

In Fig. 6, we show the far-UV luminosity predicted by FLARES at $z = 15 \rightarrow 10$ alongside both these observational constraints and other model predictions. We show both the *observed* (dust-attenuated) and *intrinsic* distribution functions. The far-UV LF follows the familiar steep decline with luminosity seen at low-redshift, dropping by roughly a factor of 10^3 from $L = 10^{28} \rightarrow 10^{29}\,\mathrm{erg\,s^{-1}\,Hz^{-1}}$. The number density of sources also evolves strongly, increasing by

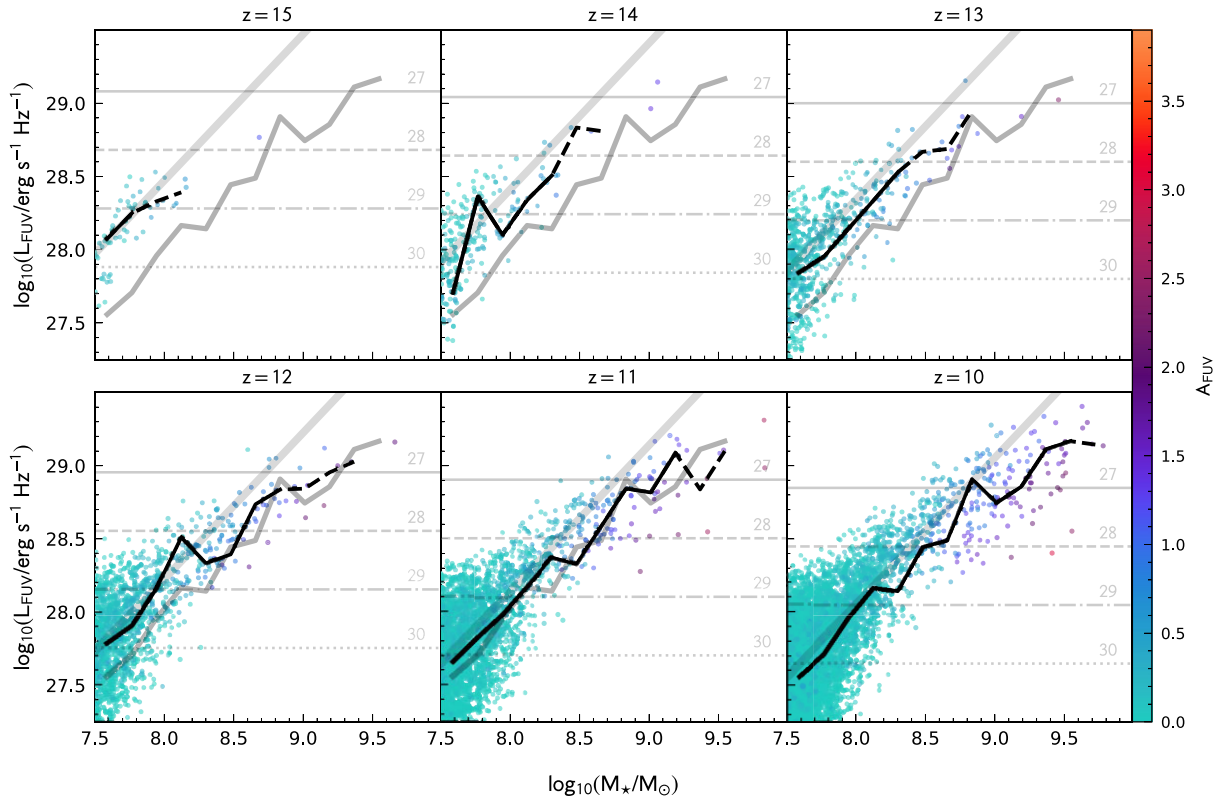

Figure 4. The relationship between stellar mass and the dust-attenuated (observed) far-UV luminosity at $z = 15 \rightarrow 10$. Points are colour-coded by the far-UV attenuation $A_{\rm FUV}$. The black line denotes the weighted median at each redshift with the line becoming dashed when the number of galaxies in each bin falls below 10. The thin grey line shows the median at $z = 10$. The thick grey line shows a weighted linear fit. Horizontal lines denote the corresponding apparent magnitude.

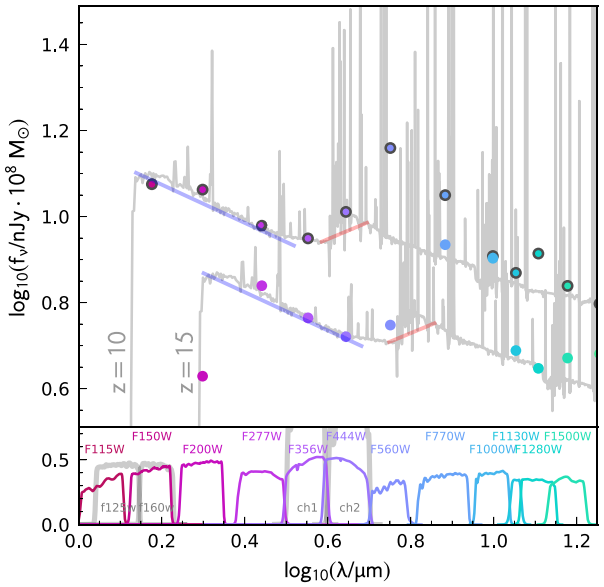

Figure 5. The observed SED of a star-forming galaxy at $z = 10$ and $z = 15$ alongside key *Hubble*, *Spitzer*, *JWST*/NIRCam, and *JWST*/MIRI filter transmission functions. Coloured points denote the predicted fluxes in each of the NIRCam and MIRI bands, highlighting the impact of nebular emission in the rest-frame optical. The blue and red lines denote the UV continuum slope and Balmer break, respectively.

$\sim 10\times$ from $z = 14 \rightarrow 10$ with stronger evolution at the bright end. At low-luminosity ($L < 10^{28.5}$ erg s^{-1} Hz^{-1}), the impact of dust is small, leaving the intrinsic and observed LF similar. However, as noted previously brighter, more massive galaxies, increasingly have stronger dust attenuation leading to a divergence in the predictions.

The $z = 10$ panel shows current observational constraints from McLeod et al. (2016), Oesch et al. (2018), and Finkelstein et al. (2021) all based on *Hubble*/WFC3 observations. While the observational uncertainties are large McLeod et al. (2016) and Oesch et al. (2018) bracket the FLARES predictions; the Oesch et al. (2018) constraints falling slightly below the predictions at low luminosities. The Finkelstein et al. (2021) constraints lie at the bright end of our predictions where dust attenuation is predicted to become important. These constraints agree better with the FLARES intrinsic predictions, possibly suggesting that too much dust is assumed in FLARES at this redshift.

Shown on the $z = 13$ panel are the recent observational constraints from Harikane et al. (2021). This study used observations from Hyper Suprime-Cam, VISTA, and *Spitzer* of the COSMOS and SXDS fields to identify a pair of bright sources with SED consistent with $z \sim 13$ star-forming galaxies. In addition, one source has a tentative line detection consistent with [O III]88 μm at $z = 13.27$, in-line with its photometric redshift. If real, these sources suggest little evolution in the bright end of the UV LF from $z \sim 10 \rightarrow 13$. FLARES contains objects with a similar space density as these sources but with dust-attenuated luminosities around a factor of $10\times$ smaller. As noted, at $z > 10$, the FLARES dust model is likely to become increasingly

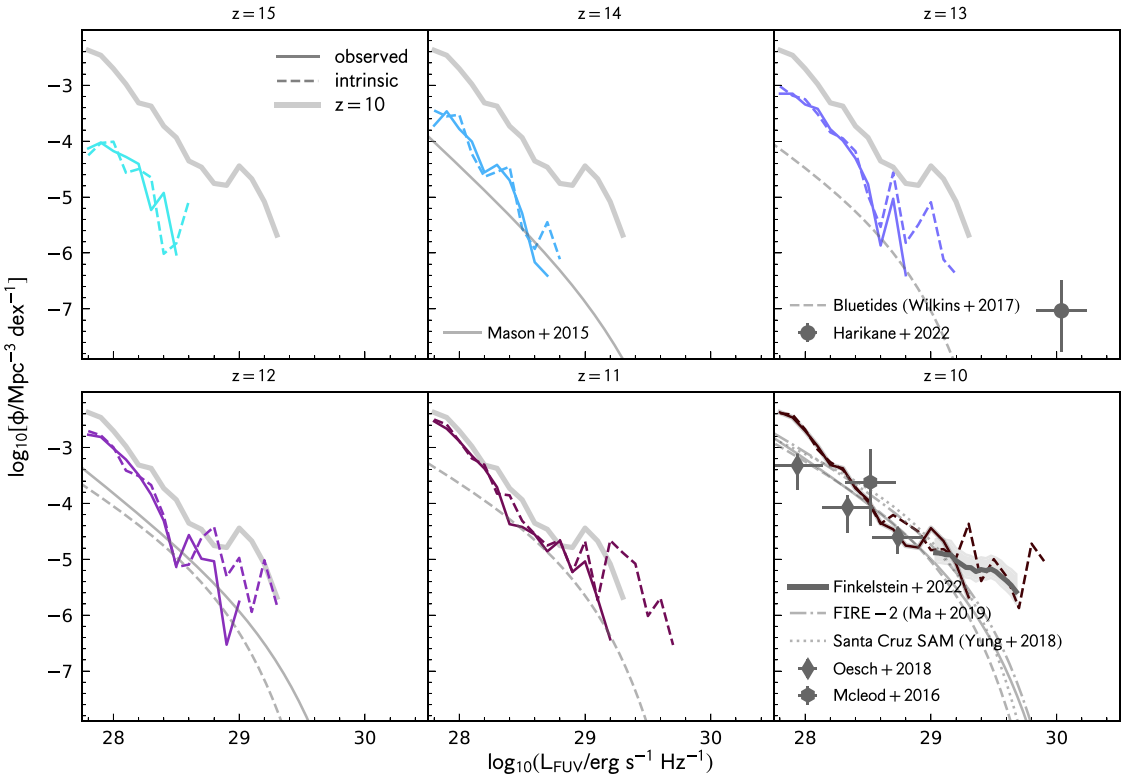

Figure 6. The observed (dust-attenuated, sold line) and intrinsic (dashed line) far-UV LF at $z = 15 \rightarrow 10$ predicted by FLARES. The thick grey line denotes the $z = 10$ prediction to more clearly demonstrate the redshift evolution. Observational constraints at $z = 10$ and $z = 13$ from McLeod et al. (2016), Oesch et al. (2018), Finkelstein et al. (2021), and Harikane et al. (2021) are also shown. Model predictions from Mason et al. (2015), Wilkins et al. (2017), Yung et al. (2019), and Ma et al. (2019) are also shown where available. These FLARES binned LFs are available in Table 1. Best-fitting Schechter parameter fits presented in Table 2, though we urge caution on their use.

Table 1. The space density of galaxies at $z = 10 \rightarrow 15$ predicted by FLARES.

$\log_{10}(L_{\rm FUV})$	ϕ/Mpc^{-3} dex^{-1}					
erg s^{-1} Hz^{-1}	$z = 15$	$z = 14$	$z = 13$	$z = 12$	$z = 11$	$z = 10$
27.8	−4.16	−3.59	−3.14	−2.78	−2.53	−2.37
28.0	−4.10	−3.64	−3.35	−3.02	−2.92	−2.67
28.2	−4.67	−4.47	−3.64	−3.45	−3.29	−3.19
28.4	−5.07	−4.71	−4.33	−4.29	−4.07	−3.65
28.6	−7.04	−6.01	−4.95	−4.83	−4.60	−4.33
28.8	−7.45	−6.71	−6.29	−5.02	−4.88	−4.56
29.0	-	−7.45	−6.12	−6.06	−5.14	−4.64
29.2	-	−6.20	−7.04	−6.12	−6.04	−4.82
29.4	-	-	-	-	−7.22	−6.68

Table 2. Best-fitting Schechter function parameters $z = 10 \rightarrow 15$ for fits to the UV LF $\log_{10}(L_{\rm FUV}/{\rm erg\,s^{-1}\,Hz^{-1}}) > 28$. Because these were defined over a narrow luminosity range, caution should be taken when using these, and we recommend using the binned LF estimates, presented in Table 1, for comparisons.

	$M_{\rm FUV}$	$\log_{10}(\phi^\star/{\rm Mpc^{-3}})$	α
$z = 15$	−20.1	−6.69	−4.2
$z = 14$	−20.3	−6.41	−4.0
$z = 13$	−20.5	−6.13	−3.8
$z = 12$	−20.7	−5.84	−3.5
$z = 11$	−20.9	−5.56	−3.3
$z = 10$	−21.0	−5.28	−3.1

unreliable since it is based on modelling calibrated at lower-redshift. However, even using intrinsic luminosities, sources with a similar space density in FLARES are still around 5× fainter, suggesting significant remaining tension.

Fig. 6 also shows a comparison with other model predictions at $z \geq 10$, including the semi-empirical model of Mason et al. (2015), the Santa Cruz semi-analytical model (Yung et al. 2019), the large-volume cosmological hydrodynamical simulation BLUETIDES (Wilkins et al. 2017), and the high-resolution FIRE-2 simulations (Ma et al. 2019). While there is good agreement at $z = 10$, the agreement with Mason et al. (2015) and BLUETIDES breaks down at high-redshift; FLARES predicts a similar density of bright galaxies but consistently predicts more faint galaxies.

4.1.1 JWST Cycle 1 forecasts

As noted in the introduction, the $z > 10$ galaxy population will soon be accessible via several deep imaging surveys conducted by *JWST*. Using our LF predictions, we can now forecast the number of sources expected for each survey and the eventual constraints on the $z = 10$–15 LF.

We begin, in Fig. 7, by presenting forecasts for the cumulative number of sources accessible to various *JWST* Cycle 1 GO, ERS, and GTO programmes. These include: CEERS, NG-DEEP,[2]

[2]Formerly Webb DEEP.

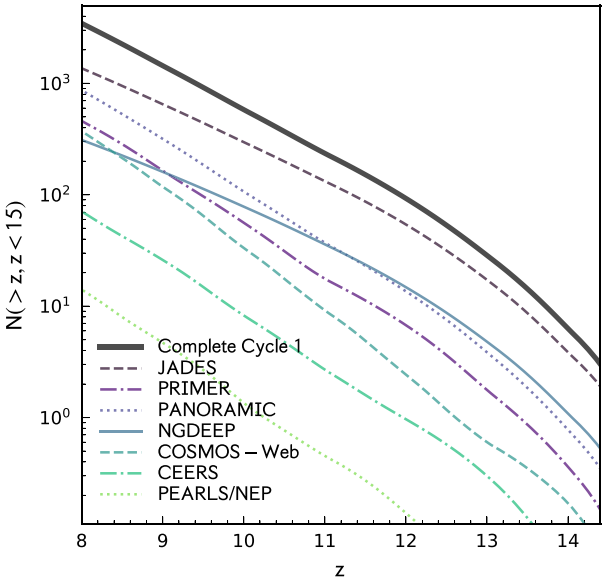

Figure 7. The cumulative number of galaxies $N(>z, z<15)$ predicted by FLARES for various *JWST* Cycle 1 GO, ERS, and GTO surveys assuming 100 per cent completeness down to the 10σ point-source F277W depth. The thick black line denotes the prediction for all surveys combined.

PRIMER, COSMOS-Web,[3] JADES, the Northern Ecliptic Pole element of PEARLS,[4] and PANORAMIC. These predictions assume 100 per cent completeness down to the 10σ point-source F277W depth, which in reality is likely to be difficult to achieve. The approximate depths/areas for each survey were provided by each programme PI except for JADES that are taken from Williams et al. (2018). Across all seven programmes, we predict ∼500, 85, and 6 galaxies at $z > 10$, $z > 12$, and $z > 14$, respectively. JADES is predicted to dominate these numbers contributing around half of expected sources at these redshifts.

In Fig. 8, we then make forecasts for the $z = 15 \rightarrow 10$ LF for the combination of the Cycle 1 programmes. The result is strong constraints at $z = 10$, comparable to the current $z = 7$ constraints from *Hubble*'s entire campaign (Bouwens et al. 2021). While these constraints progressively weaken towards higher redshift, subsequent observations throughout *JWST*'s tenure should ultimately enable useful constraints to $z \sim 15$ and potentially beyond. Crucially, this will allow us to differentiate between the different model predictions in this era.

4.2 Sizes

In Fig. 9, we present measurements of galaxy half-light radius in the far-UV for $z = 10$–12. The intrinsic size measurements are derived from the particle distribution, while the observed size measurements use a non-parametric pixel approach in which size is derived from the non-contiguous pixel area containing half the galaxy's total luminosity. The latter approach well encompasses the clumpy natures of high-redshift galaxies (e.g Jiang et al. 2013; Bowler et al. 2017). The redshift range is limited by the number of galaxies in FLARES with a sufficient number of stellar particles to make robust size measurements ($N_\star \geq 100$). As in Roper et al. (2022), we impose a 95 per cent completeness limit in each redshift bin.

Intrinsically, the high-redshift galaxy population is extremely compact with a negative size–luminosity relation. This negative trend arises from the efficient localized cooling of gas at stellar masses of $\sim 10^9$ $M_\odot$. Efficient cooling enables compact star formation, which seeds the local area with metals further aiding cooling and thus star formation. The result of this process is a feedback loop yielding compact regions with high-specific star formation rates. Galaxies that undergo this process transition from a diffuse size regime to a compact size regime with higher stellar masses/luminosities, hence the negative size–luminosity relation. This process is investigated in full in a soon-to-be-submitted work [Roper et al. (in-preparation)].

Due to the concentrated high star formation rates in the intrinsically bright central regions of these compact galaxies, they are efficiently seeding their bright cores with metals, even at this early epoch. This seeding leads to strong dust obscuration in the brightest regions, allowing the outer less enriched regions of star formation to outshine the central regions. The result of this obscuration is a larger observed size as a function of enrichment (i.e. star formation rate) and thus a positive observed size–luminosity relation.

The normalization of the observed size–luminosity relation quickly evolves at these high redshifts, with an increase of ∼0.1 dex from $z = 12$ to $z = 10$ driven by increasing obscuration of the brightest regions due to the formation of dust in the highly star-forming cores of these bright galaxies. *JWST* will not only be able to probe this obscured size–luminosity relation in the rest-frame far-UV, the reddest NIRCam filters will also be able to probe deeper into the increasingly unobscured size–luminosity relation at longer wavelengths. This will provide a valuable view into the intrinsic size–luminosity relation and its negative slope.

4.3 The UV continuum slope

The most accessible spectral diagnostic available at high-redshift is the UV continuum slope β: as can be seen in Fig. 5, the rest-frame UV continuum to $\lambda = 350$ nm is accessible to NIRCam to $z \approx 15$ and can be measured with 3–4 of NIRCam's wide filters. While primarily an indicator of dust attenuation, the UV continuum slope is also sensitive to the star formation and metal enrichment history, the Lyman continuum escape fraction, the IMF, and our understanding of stellar evolution and atmospheres[5] (e.g Wilkins et al. 2013b,a).

Fig. 10 shows predictions for β from $z = 15 \rightarrow 10$ colour-coded by the rest-frame far-UV attenuation. At $L_{\rm FUV} < 10^{28.5}$ erg s^{-1} Hz^{-1} ($M_{\rm FUV} > -19.5$), the slope is ≈ -2.4 with little evolution with redshift. At $L_{\rm FUV} > 10^{28.5}$ erg s^{-1} Hz^{-1}, the slope progressively reddens due to the increasing dust attenuation. At $L_{\rm FUV} > 10^{29}$ erg s^{-1} Hz^{-1}, the average slope has reddened to ≈ -2. Fig. 10 also shows observational constraints from Wilkins et al. (2016a); while the uncertainties are large these observations are consistent with our predictions.

The origin of the UV continuum slope is explored in more detail in Fig. 11. Here, we show the median β for unprocessed starlight (dotted line), starlight with reprocessing by gas (dashed line), and reprocessing with gas and dust (solid line, the same as that shown in Fig. 10). With no reprocessing, the predicted slopes are ≈ -2.8 at low-luminosity rising to ≈ -2.5 at $L_{\rm FUV} \approx 10^{29.5}$ erg s^{-1} Hz^{-1} with some weak ($\Delta\beta = 0.1$) evolution with redshift $z = 15 \rightarrow 10$. These trends reflect variation in the star formation and metal

[3]Formerly COSMOS-Webb.
[4]Formerly the Webb Medium Deep Fields programme (PI Windhorst).
[5]In a theoretical context, this is encapsulated in stellar population-synthesis models.

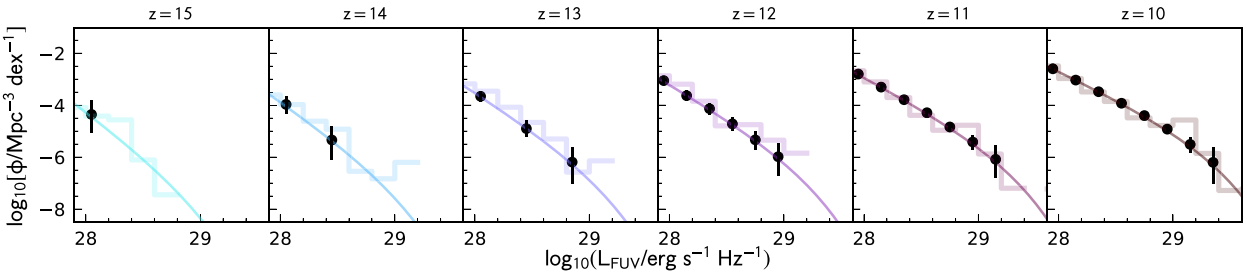

Figure 8. Predicted constraints on the UV $z = 15 \rightarrow 10$ UV LF from combined *JWST* Cycle 1 GO, ERS, and GTO surveys. Points show the forecast binned LF constraints. The stepped line shows the FLARES binned LF constraints while the smooth lines show Schechter function fits to the FLARES LF.

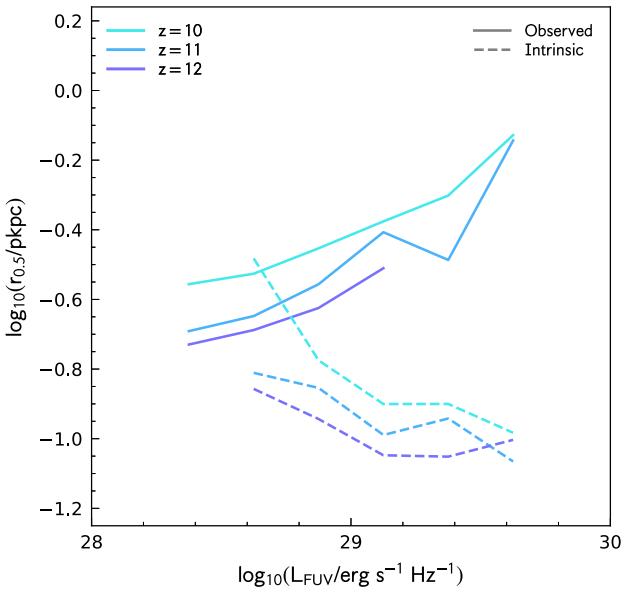

Figure 9. The redshift evolution of the size–luminosity relation predicted by FLARES in the redshift range $z = 10$–12. The lines represent the weighted 50th percentile of the galaxy distribution weighted using the FLARES weighting scheme. Solid lines show the observed size, including the effects of dust attenuation, while dashed lines show the intrinsic stellar emission. Observed sizes are measured using a non-parametric pixel approach while intrinsic sizes use a particle-based approach.

enrichment history with the brightest galaxies typically having higher metallicities. The addition of nebular (continuum) emission reddens β. As the impact of nebular emission is strongest at low metallicity, this has the effect of flattening the previous trend with luminosity and redshift leaving galaxies with $\beta \approx 2.5$. The addition of dust has an impact at all luminosities though this is most pronounced at $L_{\rm FUV} > 10^{29}$ erg s^{-1} Hz^{-1} where dust is predicted to redden the slope by $\approx$0.5.

As noted previously, the impact of dust attenuation in FLARES is particularly uncertain at $z > 10$. Recent LF constraints (i.e. Harikane et al. 2021; i.e. Finkelstein et al. 2021) tentatively suggest the presence of too much dust attenuation in FLARES. Precise constraints on the UV continuum slope from *JWST* – and ideally ALMA dust-continuum observations – in bright ($L_{\rm FUV} > 10^{29}$ erg s^{-1} Hz^{-1}) should allow us to determine whether this is the case.

4.4 UV emission lines

In addition to deep near-IR imaging, *JWST* will also be able to obtain deep near-IR spectroscopy utilizing NIRSpec, NIRCam, and NIRISS.[6] NIRSpec provides both a multi-object and integral field unit spectroscopy at 0.6–5.3 μm, while NIRCam and NIRISS together provide wide-field slit-less spectroscopy across the near-IR. At $z < 10$, this enables the observation of various strong optical lines. However, at $z > 10$, most of the strong lines fall outside the accessible range, leaving a handful of weaker UV lines. Most prominent amongst these is the [C III],C III]$\lambda\lambda$1907, 1909 Å doublet for which a handful of detections are already available at $z > 6$ (Stark et al. 2015, 2017; Topping et al. 2021).

Predictions from FLARES for the rest-frame equivalent width distribution of [C III],C III] are presented in Fig. 12 as a function of the observed (dust-attenuated) far-UV luminosity. Equivalent widths show a weak decline to higher luminosity and lower-redshift. The median value is $\approx$10 Å with the tail of the distribution reaching beyond 20 Å. Unsurprisingly, given the younger age, these predictions are offset to higher equivalent widths than observations at lower redshift (e.g Maseda et al. 2017; Llerena et al. 2022). Constraints at $z > 6$ include a handful of detections and upper limits and are likely biased due to their selection method. However, two of the detections, EGS-zs8-1 (Stark et al. 2017) and AEGIS-33376 (Topping et al. 2021), have equivalent widths at the upper extreme of the predicted distribution suggesting some possible tension. This may reflect some of the simplifying assumptions used in our modelling. For example, Wilkins et al. (2020) showed that the equivalent width of [C III],C III] is strongly sensitive to the ionization parameter and hydrogen density, for which we adopted single fiducial values.

4.5 UV – Optical colours

The near-UV – optical colour is another key spectral diagnostic of galaxies, its measurement providing insights into the star formation and metal enrichment history, dust attenuation, and nebular emission of galaxies. In the context of $z > 6$ galaxies, the near-UV – optical colour is chiefly impacted by nebular-line emission and can be used to infer the strength of combination of the Hβ and [O III] lines (e.g De Barros et al. 2019b; Endsley et al. 2021). When a spectroscopic redshift is available, it is sometimes possible to avoid strong line emission, thereby providing 'clean' constraints on the strength of the Balmer break (e.g. Hashimoto et al. 2018) and thus a more accurate constraint on the star formation and metal enrichment history. For a wider introduction to the break in the context of the high-redshift Universe, see Wilkins et al. in preparation.

In principle, *JWST* can observe the rest-frame optical to $z = 15$ and beyond. However, at $z > 11$, the optical falls beyond the range

[6]MIRI also has spectroscopic capabilities but has much lower sensitivity and only target galaxies individually.

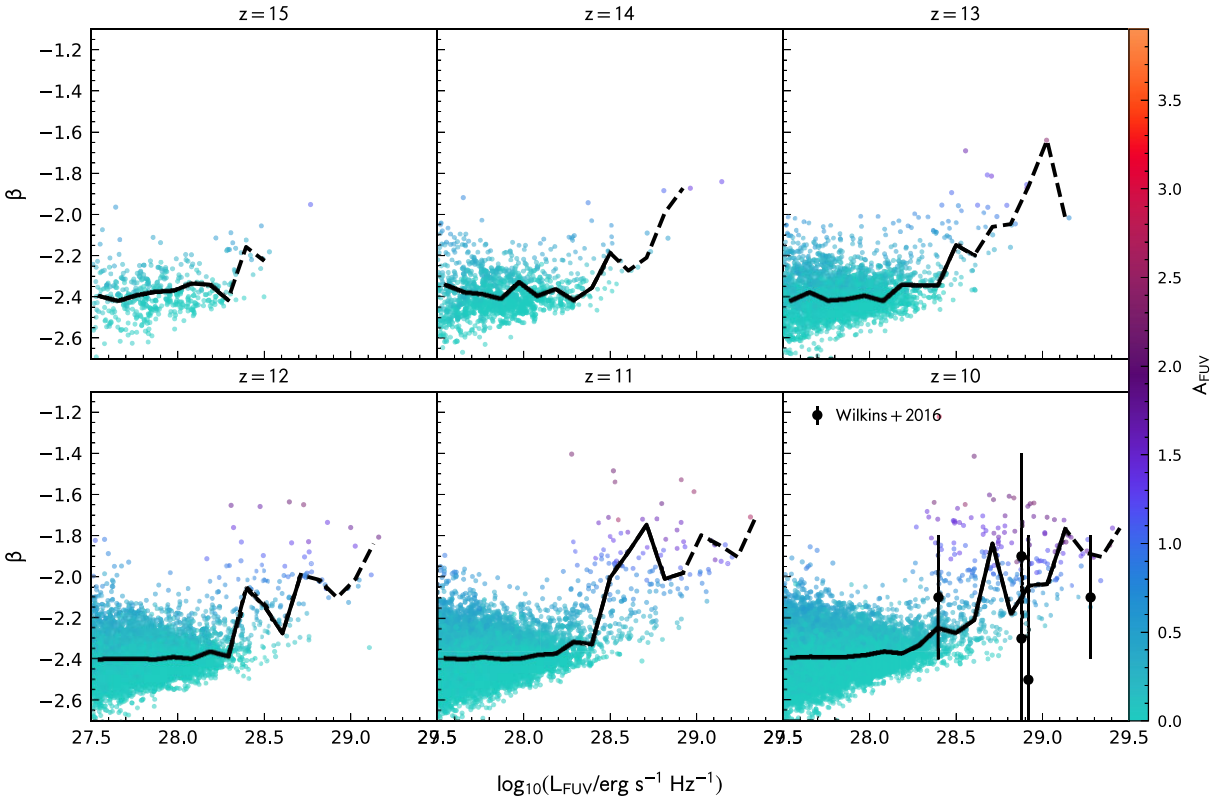

Figure 10. The rest-frame UV continuum slope β as a function of far-UV luminosity at $z = 15 \rightarrow 10$. Individual galaxies are colour-coded by their far-UV attenuation. The solid (dashed) black line shows the median value for bins with $\geq$10 ($<$10) galaxies. Observational constraints from Wilkins et al. (2016a) are also shown at $z = 10$.

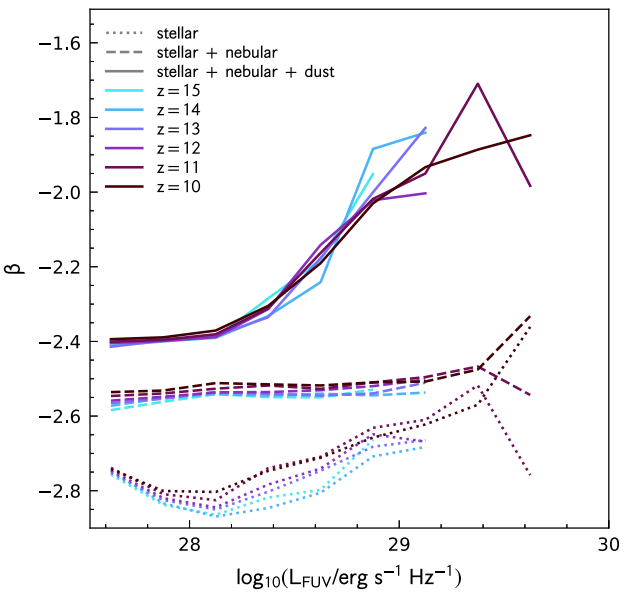

Figure 11. The average UV continuum slope as a function of UV luminosity and redshift. The dotted line shows the UV continuum slope predicted from just the pure stellar emission while the dashed line also includes nebular emission and the solid line includes both nebular emission and dust (i.e. that which would be observed).

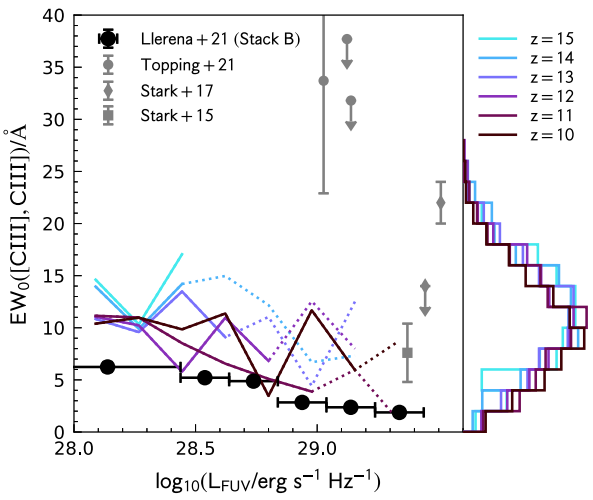

Figure 12. The distribution of [C III],C III]$\lambda\lambda$1907, 1909 Å equivalent widths at $z = 10$–15 predicted by FLARES. Also shown are stacked results at $z \approx 3$ from the VANDELS survey (Llerena et al. 2022) and individual objects at $z > 6$ (Stark et al. 2015, 2017; Topping et al. 2021).

accessible to *JWST*'s near-IR instruments and thus requires MIRI observations. Several blind-field cycle 1 surveys will simultaneously collect both multiband NIRCam and MIRI imaging. For MIRI, F770W is the most popular choice and with this in mind, we present the predicted F444W-F770W colour in Fig. 13. We do this for both the pure stellar photometry and the photometry, including nebular emission and dust. In both cases, there is little trend with the UV luminosity. The addition of nebular emission (and dust) has the

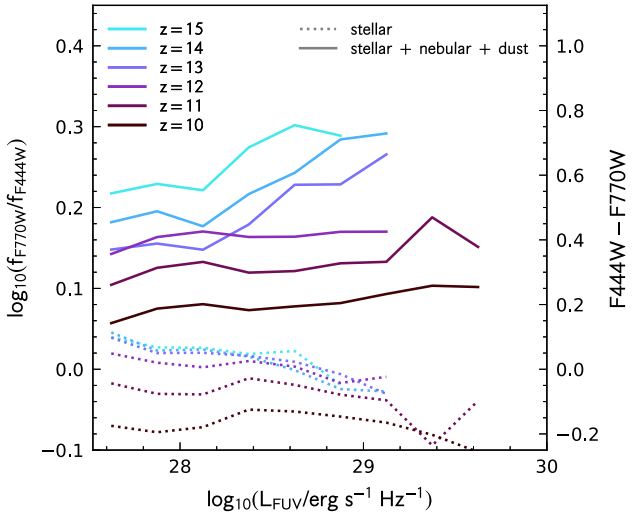

Figure 13. The average NIRCam/F444W – MIRI/F770W colour as a function of UV luminosity for both the pure stellar emission (dotted line) and including nebular emission and dust (solid line).

impact of significantly reddening the colour by ≈0.4 mag at $z = 10$ increasing to ≈0.7 mag at $z = 15$. This reflects both the increasing optical line equivalent widths but also the lines that fall within the F770W band.

While in principle, MIRI observations, when combined with NIRCam, should thus allow us to constrain optical line emission at $z > 10$, unfortunately MIRI has both a lower sensitivity[7] and smaller field of view than NIRCam resulting in a much reduced survey efficiency. Blind field cycle 1 programmes (i.e. PRIMER, COSMOS-Web, and CEERS) obtaining both NIRCam and MIRI F770W observations typically reach depths F770W 3 mag shallower than the deepest NIRCam observations and only over less than half the total area. Combined with the expected surface densities and flux distributions, it is then unlikely, even with stacking, that MIRI will yield useful constraints at $z > 10$. However, there is the possibility of obtaining deep MIRI imaging of individual bright targets in later cycles.

5 CONCLUSIONS

In this article, we have presented theoretical predictions for the properties of galaxies at $z = 10$–15 from the FLARES. These are amongst the first predictions from a cosmological hydrodynamical simulation calibrated at $z = 0$ at these redshifts enabled by the unique simulation strategy adopted by FLARES. Our major findings are:

(i) Specific star formation rates and ages show little trend with stellar mass though evolve strongly with redshift. However, gas-phase metallicities and dust attenuation rapidly increase with stellar mass but show little redshift evolution.

(ii) The far-UV LF continues its evolution from lower-redshift with the luminosity density predicted to drop by ∼10 × from $z = 10 \rightarrow 14$. At $z = 10$, the predictions are consistent with observational constraints from McLeod et al. (2016), Oesch et al. (2018), and Finkelstein et al. (2021) though favour less dust attenuation. FLARES contains galaxies with a similar space density to those recently identified by Harikane et al. (2021) but ∼5–10× fainter depending on whether dust attenuation is included. Similarly, agreement with other models is good at $z = 10$ but diverges to higher-redshift with FLARES, predicting more faint galaxies than other models. Based on these predictions in cycle 1 alone *JWST* should identify ∼600, 100, and 6 galaxies at $z > 10$, 12, and 14, respectively, providing robust constraints on the LF to $z \sim 13$.

(iii) FLARES predicts little redshift evolution in the relationship between the UV continuum slope β and UV luminosity. The brightest galaxies are predicted to be moderately reddened ($\Delta\beta \approx 0.5$) by dust.

(iv) UV-optical colours probed by NIRCam and MIRI are likely to be dominated by nebular emission though will be hard to measure due to MIRI's much lower sensitivity.

[7]In 10 ks, NIRCam can reach in 9.1 and 23.6 nJy in the F200W and F444W bands, respectively, while for the MIRI F560W and F770W bands, the flux sensitivity is 130 and 240 nJy.

ACKNOWLEDGEMENTS

We dedicate this article to healthcare and other essential workers, the teams involved in developing the vaccines, and to all the parents who found themselves having to home-school children while holding down full-time jobs. We thank the EAGLE team for their efforts in developing the EAGLE simulation code. This work used the DiRAC@Durham facility managed by the Institute for Computational Cosmology on behalf of the STFC DiRAC HPC Facility (www.dirac.ac.uk). The equipment was funded by BEIS capital funding via STFC capital grants ST/K00042X/1, ST/P002293/1, ST/R002371/1, and ST/S002502/1, Durham University and STFC operations grant ST/R000832/1. DiRAC is part of the National e-Infrastructure. CCL acknowledges support from the Royal Society under grant RGF/EA/181016. DI acknowledges support by the European Research Council via ERC Consolidator Grant KETJU (no. 818930). The Cosmic Dawn Center (DAWN) is funded by the Danish National Research Foundation under grant No. 140. We also wish to acknowledge the following open source software packages used in the analysis: NUMPY (Harris et al. 2020), SCIPY (Virtanen et al. 2020), and MATPLOTLIB (Hunter 2007). This research made use of ASTROPY http://www.astropy.org a community-developed core PYTHON package for Astronomy (Astropy Collaboration 2013, 2018). Parts of the results in this work make use of the colourmaps in the CMASHER package (van der Velden 2020).

DATA AVAILABILITY STATEMENT

Binned data for making easy comparisons are available in `ascii` formats at https://github.com/stephenmwilkins/flares_frontier_data. Data from the wider FLARES project are available at https://flaresimulations.github.io/data.html. If you use data from this paper, please also cite Lovell et al. (2021) and Vijayan et al. (2021).

REFERENCES

Astropy Collaboration, 2013, A&A, 558, A33
Astropy Collaboration, 2018, AJ, 156, 123
Barnes D. J. et al., 2017, MNRAS, 471, 1088
Behroozi P. et al., 2020, MNRAS, 499, 5702
Bernardini M., Feldmann R., Anglés-Alcázar D., Boylan-Kolchin M., Bullock J., Mayer L., Stadel J., 2022, MNRAS, 509, 1323
Bouwens R. J. et al., 2010, ApJ, 709, L133
Bouwens R. J. et al., 2012, ApJ, 754, 83
Bouwens R. J. et al., 2014, ApJ, 793, 115
Bouwens R. J. et al., 2015, ApJ, 803, 34
Bouwens R. J. et al., 2021, AJ, 162, 47
Bowler R. A. A. et al., 2015, MNRAS, 452, 1817

Bowler R. A. A., Dunlop J. S., McLure R. J., McLeod D. J., 2017, MNRAS, 466, 3612
Bunker A. J. et al., 2010, MNRAS, 409, 855
Calzetti D., Armus L., Bohlin R. C., Kinney A. L., Koornneef J., Storchi-Bergmann T., 2000, ApJ, 533, 682
Caruana J., Bunker A. J., Wilkins S. M., Stanway E. R., Lorenzoni S., Jarvis M. J., Ebert H., 2014, MNRAS, 443, 2831
Chabrier G., 2003, PASP, 115, 763
Clay S. J., Thomas P. A., Wilkins S. M., Henriques B. M. B., 2015, MNRAS, 451, 2692
Crain R. A. et al., 2009, MNRAS, 399, 1773
Crain R. A. et al., 2015, MNRAS, 450, 1937
Curtis-Lake E. et al., 2012, MNRAS, 422, 1425
Davé R., Anglés-Alcázar D., Narayanan D., Li Q., Rafieferantsoa M. H., Appleby S., 2019, MNRAS, 486, 2827
Davis M., Efstathiou G., Frenk C. S., White S. D. M., 1985, ApJ, 292, 371
Dayal P., Ferrara A., 2018, Phys. Rep., 780, 1
De Barros S., Oesch P. A., Labbé I., Stefanon M., González V., Smit R., Bouwens R. J., Illingworth G. D., 2019a, MNRAS, 489, 2355
De Barros S., Oesch P. A., Labbé I., Stefanon M., González V., Smit R., Bouwens R. J., Illingworth G. D., 2019b, MNRAS, 489, 2355
Dolag K., Borgani S., Murante G., Springel V., 2009, MNRAS, 399, 497
Endsley R., Stark D. P., Chevallard J., Charlot S., 2021, MNRAS, 500, 5229
Feng Y., Di-Matteo T., Croft R. A., Bird S., Battaglia N., Wilkins S., 2016, MNRAS, 455, 2778
Ferland G. J. et al., 2017, Rev. Mex. Astron. Astrofis., 53, 385
Finkelstein S. L. et al., 2015, ApJ, 810, 71
Finkelstein S. L. et al., 2021, ApJ, 928, 52
Genel S. et al., 2014, MNRAS, 445, 175
Harikane Y. et al., 2021, ApJ, 929, 1
Harris C. R. et al., 2020, Nature, 585, 357
Hashimoto T. et al., 2018, Nature, 557, 392
Hashimoto T. et al., 2019, PASJ, 71, 71
Hunter J. D., 2007, Comput. Sci. Eng., 9, 90
Hutter A., Dayal P., Yepes G., Gottlöber S., Legrand L., Ucci G., 2021, MNRAS, 503, 3698
Jiang L. et al., 2013, ApJ, 773, 153
Kannan R., Garaldi E., Smith A., Pakmor R., Springel V., Vogelsberger M., Hernquist L., 2022, MNRAS, 511, 4005
Kennicutt R. C., Evans N. J., 2012, ARA&A, 50, 531
Khandai N., Feng Y., DeGraf C., Di Matteo T., Croft R. A. C., 2012, MNRAS, 423, 2397
Knudsen K. K., Richard J., Kneib J.-P., Jauzac M., Clément B., Drouart G., Egami E., Lindroos L., 2016, MNRAS, 462, L6
Llerena M. et al., 2022, A&A, 659, A16
Lovell C. C., Vijayan A. P., Thomas P. A., Wilkins S. M., Barnes D. J., Irodotou D., Roper W., 2021, MNRAS, 500, 2127
Lovell C. C., Wilkins S. M., Thomas P. A., Schaller M., Baugh C. M., Fabbian G., Bahé Y., 2022, MNRAS, 509, 5046
Ma X. et al., 2019, MNRAS, 487, 1844
Marinacci F. et al., 2018, MNRAS, 480, 5113
Maseda M. V. et al., 2017, A&A, 608, A4
Mason C. A., Trenti M., Treu T., 2015, ApJ, 813, 21
Mason C. A. et al., 2019, MNRAS, 485, 3947
McLeod D. J., McLure R. J., Dunlop J. S., 2016, MNRAS, 459, 3812
McLure R. J., Dunlop J. S., Cirasuolo M., Koekemoer A. M., Sabbi E., Stark D. P., Targett T. A., Ellis R. S., 2010, MNRAS, 403, 960
Naiman J. P. et al., 2018, MNRAS, 477, 1206
Nelson D. et al., 2018, MNRAS, 475, 624
Ni Y. et al., 2022, MNRAS, 513, 670
O'Shea B. W., Wise J. H., Xu H., Norman M. L., 2015, ApJ, 807, L12
Ocvirk P. et al., 2016, MNRAS, 463, 1462
Ocvirk P. et al., 2020, MNRAS, 496, 4087
Oesch P. A. et al., 2016, ApJ, 819, 129
Oesch P. A., Bouwens R. J., Illingworth G. D., Labbé I., Stefanon M., 2018, ApJ, 855, 105
Pei Y. C., 1992, ApJ, 395, 130
Pentericci L. et al., 2014, ApJ, 793, 113
Pentericci L. et al., 2016, ApJ, 829, L11
Pillepich A. et al., 2018, MNRAS, 475, 648
Planck Collaboration, 2014, A&A, 571, A1
Poole G. B., Angel P. W., Mutch S. J., Power C., Duffy A. R., Geil P. M., Mesinger A., Wyithe S. B., 2016, MNRAS, 459, 3025
Robertson B. E., 2021, A&A, 60, 121
Roper W. J., Lovell C. C., Vijayan A. P., Marshall M. A., Irodotou D., Kuusisto J. K., Thomas P. A., Wilkins S. M., 2022, MNRAS, 514, 1921
Rosdahl J. et al., 2018, MNRAS, 479, 994
Schaye J. et al., 2015, MNRAS, 446, 521
Schenker M. A., Ellis R. S., Konidaris N. P., Stark D. P., 2014, ApJ, 795, 20
Sijacki D., Vogelsberger M., Genel S., Springel V., Torrey P., Snyder G. F., Nelson D., Hernquist L., 2015, MNRAS, 452, 575
Springel V., White S. D. M., Tormen G., Kauffmann G., 2001, MNRAS, 328, 726
Springel V. et al., 2018, MNRAS, 475, 676
Stanway E. R., Eldridge J. J., 2018, MNRAS, 479, 75
Stark D. P., Ellis R. S., Chiu K., Ouchi M., Bunker A., 2010, MNRAS, 408, 1628
Stark D. P. et al., 2015, MNRAS, 450, 1846
Stark D. P. et al., 2017, MNRAS, 464, 469
Topping M. W., Shapley A. E., Stark D. P., Endsley R., Robertson B., Greene J. E., Furlanetto S. R., Tang M., 2021, ApJ, 917, L36
van der Velden E., 2020, J. Open Sour. Softw., 5, 2004
Vijayan A. P., Clay S. J., Thomas P. A., Yates R. M., Wilkins S. M., Henriques B. M., 2019, MNRAS, 489, 4072
Vijayan A. P., Lovell C. C., Wilkins S. M., Thomas P. A., Barnes D. J., Irodotou D., Kuusisto J., Roper W. J., 2021, MNRAS, 501, 3289
Vijayan A. P. et al., 2022, MNRAS, 511, 4999
Virtanen P. et al., 2020, Nature Methods, 17, 261
Vogelsberger M. et al., 2014a, MNRAS, 444, 1518
Vogelsberger M. et al., 2014b, Nature, 509, 177
Vogelsberger M. et al., 2020, MNRAS, 492, 5167
Wilkins S. M., Bunker A. J., Lorenzoni S., Caruana J., 2011, MNRAS, 411, 23
Wilkins S. M., Bunker A., Coulton W., Croft R., di Matteo T., Khandai N., Feng Y., 2013a, MNRAS, 430, 2885
Wilkins S. M. et al., 2013b, MNRAS, 435, 2885
Wilkins S. M., Bouwens R. J., Oesch P. A., Labbé I., Sargent M., Caruana J., Wardlow J., Clay S., 2016a, MNRAS, 455, 659
Wilkins S. M., Feng Y., Di-Matteo T., Croft R., Stanway E. R., Bouwens R. J., Thomas P., 2016b, MNRAS, 458, L6
Wilkins S. M., Feng Y., Di-Matteo T., Croft R., Stanway E. R., Bunker A., Waters D., Lovell C., 2016c, MNRAS, 460, 3170
Wilkins S. M., Feng Y., Di Matteo T., Croft R., Lovell C. C., Waters D., 2017, MNRAS, 469, 2517
Wilkins S. M., Feng Y., Di Matteo T., Croft R., Lovell C. C., Thomas P., 2018, MNRAS, 473, 5363
Wilkins S. M., Lovell C. C., Stanway E. R., 2019, MNRAS, 490, 5359
Wilkins S. M. et al., 2020, MNRAS, 493, 6079
Williams C. C. et al., 2018, ApJS, 236, 33
Yung L. Y. A., Somerville R. S., Finkelstein S. L., Popping G., Davé R., 2019, MNRAS, 483, 2983

This paper has been typeset from a TEX/LATEX file prepared by the author.